JOURNAL OF PROPULSION AND POWER
Vol. 25, No. 1, January–February 2009

Feasibility of an Onboard Surface Hall Magnetohydrodynamic Power Generator in Reentry Flight

Takayasu Fujino* and Motoo Ishikawa†
University of Tsukuba, Tsukuba 305-8573, Japan

DOI: 10.2514/1.33354

The feasibility of electrical power extraction in Earth-reentry flights by using an onboard surface Hall-type magnetohydrodynamic power generator is numerically examined by using an axisymmetric two-dimensional magnetohydrodynamic code, which accounts for the thermochemical nonequilibrium states and the Hall effect. The present study assumes that a reentry body with a nose radius of 1.35 m is equipped with a pair of electrodes on the wall surface for extracting electrical power produced by the Hall effect. Numerical results demonstrate that the onboard surface Hall-type magnetohydrodynamic power generator can extract the electrical power above 1 MW by applying the magnetic field of 0.3–0.5 T at an altitude of about 60 km and a flight velocity of about 5.6 km/s. The numerical results also show that the heat flux to the body is further suppressed by the applied magnetic field when the load voltage between electrodes is increased. This is because an increase of load voltage leads to a strengthening of the magnetohydrodynamic interaction.

Nomenclature

$\boldsymbol{B}$	=	magnetic field vector, T
B_r, B_z	=	components of magnetic flux density in the r and z directions, T
B_0	=	magnetic flux density at the stagnation point, T
D_s	=	effective diffusion coefficient of species s, m^2/s
$\hat{D}_s$	=	average vibrational energy of molecule s, which is created or destroyed at rate $\dot{\omega}_s$, J/kmol
E	=	total energy, J/kg^3
$\boldsymbol{E}$	=	electric field vector, V/m
E_r, E_z	=	components of electric field in the r and z directions, V/m
e	=	electronic charge, C
$\boldsymbol{e_r}$, $\boldsymbol{e_z}$	=	unit vectors in the r and z directions
e_{ve}	=	vibrational-electronic-electron energy, J/kg
$e_{v,s}$	=	vibrational energy of species s, J/kg
$e^*_{v,s}$	=	equilibrium vibrational energy of species s, J/kg
H	=	total enthalpy, J/kg
h_s	=	enthalpy of species s, J/kg
$h_{\text{ve},s}$	=	vibrational-electronic-electron enthalpy of species s, J/kg
I	=	load current, A
I_s	=	first ionization energy of species s, J/kmol
$\boldsymbol{J}$	=	vector of electric current density, A/m^2
J_r, J_θ, J_z	=	components of electric current density in the r, θ, and z directions, A/m^2
k_b	=	Boltzmann's constant, J/K
$k_{b,i}$	=	backward reaction rate coefficient for reaction i, $m^3/(\text{kmol}\cdot\text{s})$ or $m^6/(\text{kmol}^2\cdot\text{s})$
$k_{f,i}$	=	forward reaction rate coefficient for reaction i, $m^3/(\text{kmol}\cdot\text{s})$
M_e	=	molecular weight of an electron, kg/kmol
M_s	=	molecular weight of species s, kg/kmol
m_e	=	mass of an electron, kg
n_e	=	number density of an electron, $1/m^3$
n_s	=	number density of species s, $1/m^3$
$\dot{n}_{e,s}$	=	molar rate of production of species s by electron impact ionization, $\text{kmol}/(m^3\cdot\text{s})$
P_∞	=	freestream pressure, Pa
p	=	static pressure, Pa
p_e	=	partial pressure of an electron, Pa
p_s	=	partial pressure of species s, Pa
R	=	universal gas constant, $J/(\text{kmol}\cdot\text{K})$
R_b	=	nose radius of the body, m
R_{ext}	=	external load resistance, Ω
$R_{f,i}$, $R_{b,i}$	=	forward and backward reaction rates for reaction i, $\text{kmol}/(m^3\cdot\text{s})$
r, θ, z	=	cylindrical coordinates
T_{tr}	=	translational-rotational temperature, K
T_{ve}	=	vibrational-electronic-electron temperature, K
T_W	=	wall temperature, K
T_∞	=	freestream temperature, K
t	=	time, s
U_∞	=	freestream velocity, m/s
u_r, u_θ, u_z	=	velocity components in the r, θ, and z directions, m/s
V_L	=	load voltage, V
y_s	=	mole fraction of species s
$\alpha_{s,i}$, $\beta_{s,i}$	=	forward and backward stoichiometric coefficients of species s in reaction i
β	=	electron Hall parameter
ε_0	=	permittivity of vacuum, F/m
η_{tr}	=	mixture translational-rotational thermal conductivity, $W/(m\cdot K)$
η_{ve}	=	mixture vibrational-electron thermal conductivity, $W/(m\cdot K)$
μ	=	mixture viscosity, $\text{kg}/(m\cdot\text{s})$
$\nu_{e,s}$	=	effective energy exchange collision frequency of an electron with species s, $1/s$
$\nu^m_{e,s}$	=	effective momentum transfer collision frequency of an electron with species s, $1/s$
ξ, η	=	generalized curvilinear coordinates
ρ	=	total mass density, kg/m^3
ρ_e	=	mass density of an electron, kg/m^3
ρ_s	=	mass density of species s, kg/m^3
σ	=	electrical conductivity, S/m
$\sigma_{e,s}$	=	effective collision cross section of electrons with neutral species s, m^2
$\tau_{i,j}$	=	viscous shear stress

Presented as Paper 4248 at the 38th AIAA Plasmadynamics and Lasers Conference in conjunction with the 16th International Conference on MHD Energy Conversion, Miami, FL, 25–28 June 2007; received 10 July 2007; accepted for publication 20 September 2008.

*Assistant Professor, Graduate School of Systems and Information Engineering. Member AIAA.

†Professor, Graduate School of Systems and Information Engineering. Senior Member AIAA.

τ_s = translational-vibrational energy relaxation time of species s, s
ϕ = electric potential, V
ϕ_{anode} = electric potential on an anode electrode, V
ϕ_{cathode} = electric potential on a cathode electrode, V
$\dot{\omega}_s$ = mass production rate of species s, kg/(m^3 · s)
$\dot{\omega}_{\text{ve}}$ = production rate of vibrational-electronic-electron energy, J/(m^3 · s)

I. Introduction

A NUMBER of feasibility studies on applications of magnetohydrodynamic (MHD) technology to the aerospace engineering field have been conducted both numerically and experimentally by many researchers in the United States, Russia, Japan, and many other nations.

As one of the MHD applications, the active thermal protection technique in reentry flights using the MHD technology, which is called the MHD thermal protection or the MHD heat shield, was proposed in the 1950s (for example, see [1–3]). The outline of the concept of the MHD thermal protection is as follows: when the magnetic field, which is produced by a magnet system installed in a space vehicle, is applied to the weakly ionized plasma flow in the shock layer, the electric current is produced in the shock layer. The interaction between the electric current and the applied magnetic field induces the Lorentz force in the shock layer. The Lorentz force decelerates the plasma flow in the shock layer and increases the thickness of the shock layer. Consequently, the aerodynamic heating can be reduced.

Using numerical simulation, we have examined the feasibility of MHD thermal protection [4–6] in recent years. The numerical studies have been conducted mainly under the OREX (Orbital Reentry Experiments) reentry experimental flight condition at an altitude of about 60 km, where it was observed during the OREX experiment (Japan, 1994) that the aerodynamic heating peaked [7]. These studies showed that applying a magnetic field of about 0.5 T reduced the wall heat flux at the stagnation point by about 80% compared with the value obtained in the absence of the applied magnetic field and that the Hall parameter in the shock layer was greater than 10. Moreover, it was found that the Hall effect dominated the electrodynamics in the shock layer. Figures 1 and 2 illustrate the streamlines of electric current and the distribution of electric potential, respectively, ahead of the axisymmetric r–z two-dimensional blunt-body OREX with a nose radius of 1.35 m when the dipole magnetic field of about 0.5 T with the r and z components is applied. These figures were obtained in our previous numerical study of the MHD thermal protection [5], showing that the Hall effect induces the electric current with the r and z components, as well as the azimuthal θ component, and also

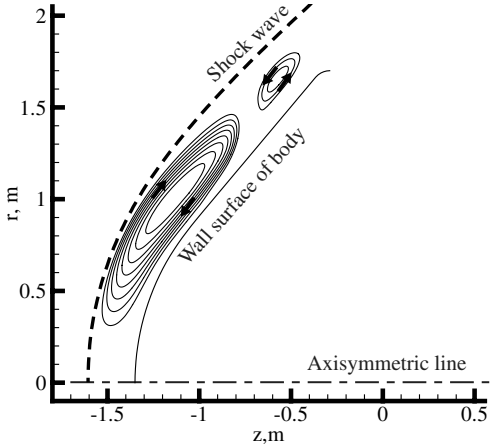

Fig. 1 Streamlines of electric current on the r–z plane induced by the Hall effect obtained in the authors' previous study [5]. Note that the streamlines are the same as those in the case without electrodes for the parameter $B_0 = 0.5$ T in the present study.

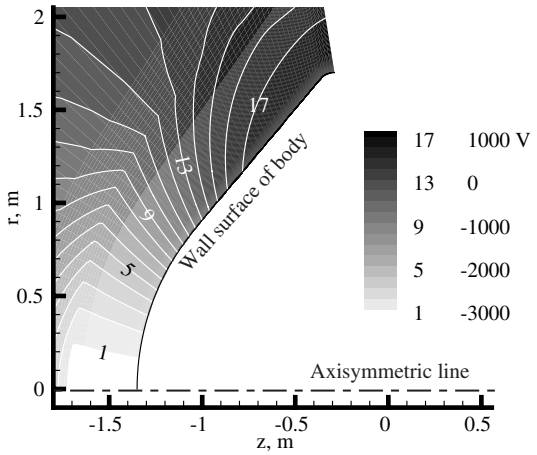

Fig. 2 Distribution of electric potential on the r–z plane induced by the Hall effect obtained in the authors' previous study [5]. Note that its distribution is the same as that in the case without electrodes for the parameter $B_0 = 0.5$ T in the present study.

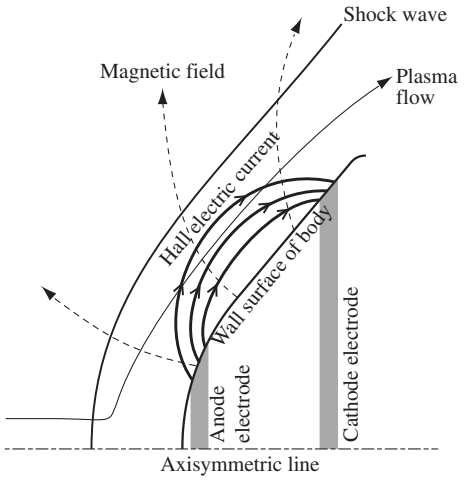

Fig. 3 Concept of onboard surface Hall-type MHD power generator for extracting electric power in reentry flights.

induces the electric potential elevation of about 4 kV from the stagnation point to the shoulder of the body. These results therefore suggest that there is a possibility of electrical power extraction during reentry flights by the principle of the Hall-type MHD power generation if a pair of electrodes can be placed on the wall surface of a space vehicle, as shown in Fig. 3.

The concept of onboard surface MHD power generators during reentry flights was proposed by Bityurin et al. [8]. They also suggested, as an example of the usages of extracted electrical power, that the extracted electrical power could be used by a flight control system to optimize reentry trajectories and particular maneuvers.

Recently, Macheret et al. [9] theoretically explored the possibility of onboard surface MHD power generators during Earth-reentry flights, and they concluded that the substantial amounts of electrical power from several hundred kilowatts to a few megawatts per square meter from the surface at altitudes of 45–60 km and flight velocities of 6–7 km/s can be extracted with a modest amount (1%) of alkali seed and applied magnetic field of 0.1–0.2 T. Their research group has continued feasibility studies on this onboard surface MHD power generator using a more sophisticated three-dimensional computational code including finite rate ionization model [10,11].

The theoretical study carried by Macheret et al. [9] proposed to use the Faraday-type MHD power generator. By contrast, the type of the onboard surface MHD power generator proposed in the present study is classified as a Hall-type MHD power generator, as shown in Fig. 3. The feasibility of electrical power extraction in reentry flights by

using the onboard surface Hall-type MHD power generator has not been explored before.

The purpose of the present study, therefore, is to numerically demonstrate the proof of the concept for extracting electric power during reentry flights by using the onboard surface Hall-type MHD power generator. Moreover, the present study numerically examines the influence of the applied magnetic field on the wall heat flux when the electric power is extracted by the onboard surface Hall-type MHD power generator.

II. Numerical Methods and Numerical Conditions

A. Blunt Body Equipped with a Pair of Electrodes for Extracting Electrical Power

Figure 4 illustrates a configuration of a blunt body with a pair of electrodes for constructing an onboard surface Hall-type MHD power generator. The shape of the blunt body is the same as that of the blunt-body OREX used in the reentry experiments in Japan (1994) [7]. The forebody shape is composed of a spherical nose with a radius of 1.35 m, a cone, and a circular shoulder. The computational region is only the region ahead of the blunt body. The present study assumes that the load resistance into the blunt body is connected between two electrodes and that the load voltage is adjusted by varying the value of the load resistance.

Although the present study assumes that the anode electrode is placed on the wall surface around the stagnation point at which the aerodynamic heating is severest, the anode electrode should be kept away from the stagnation point when considering the thermal problem. We will therefore conduct numerical studies of optimizing the configuration of electrodes when considering the generator performance as well as the thermal problem in our near-future study.

B. Flight Condition and Applied Magnetic Field Condition

The present numerical simulations are carried out under the flight condition at the altitude of about 60 km in the OREX experiments as follows: the freestream pressure P_∞ is 23.6 Pa, the freestream temperature T_∞ is 248.1 K, and the freestream velocity U_∞ is 5562 m/s [7]. Under the flight condition, the aerodynamic heating had a peak value in the OREX experiments. It is well known that the electrical conductivity and the Hall parameter, which directly affect the generator performance, strongly depend on flight conditions. We are therefore planning to examine the influence of flight conditions on the generator performance for wide flight conditions in a near-future study.

An externally applied magnetic field is assumed to be produced by a dipole magnet placed at the point of $r = 0$ m and $z = 0$ m inside the blunt body:

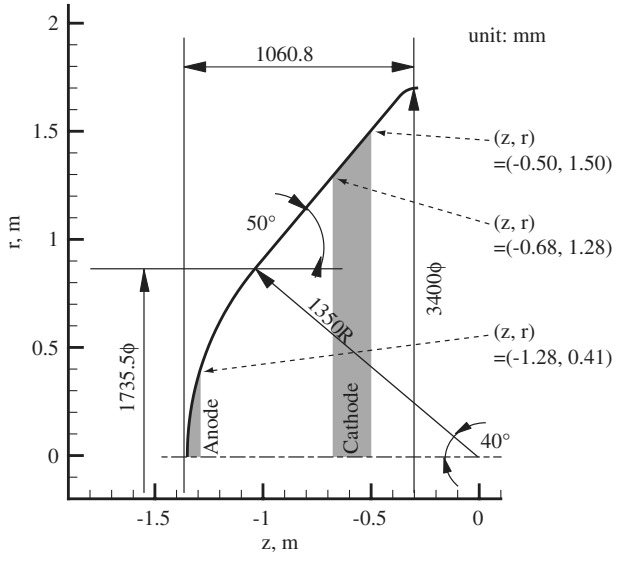

Fig. 4 Configuration of a blunt body with a pair of electrodes for constructing onboard surface Hall-type MHD power generator.

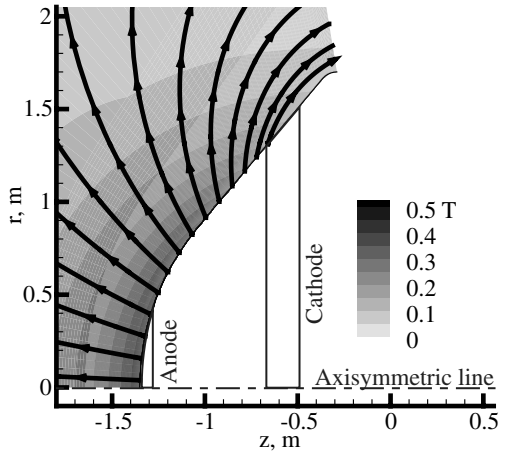

Fig. 5 Distribution of the applied magnetic field for the parameter $B_0 = 0.5$ T.

$$\boldsymbol{B}(r,z) = -\frac{B_0 R_b^3}{2(z^2+r^2)^{3/2}}\left[\left(\frac{2z^2}{z^2+r^2}-\frac{r^2}{z^2+r^2}\right)\boldsymbol{e}_z + \frac{3zr}{z^2+r^2}\boldsymbol{e}_r\right] \tag{1}$$

In the present study, the parameter B_0 in Eq. (1) is varied over a range of 0.3 to 0.5 T to examine influences of the strength of the applied magnetic field on the generator performance and the wall heat flux. Figure 5 shows a distribution of the applied magnetic field for the parameter $B_0 = 0.5$ T.

C. Basic Equations for Gasdynamics and Electrodynamics

The present study regards the flowfield and the electromagnetic field as an axisymmetric two-dimensional field (r–z). The basic equations for the gasdynamics are the mass conservation equations of chemical species, the momentum-conservation equations, the total-energy-conservation equation, and the vibrational-electronic-electron energy-conservation equation. We consider the following 11 chemical species: N, O, N_2, O_2, NO, N^+, O^+, N_2^+, O_2^+, NO^+, and e^-. As a finite rate chemical kinetics model, we use Kang et al.'s [12] model, in which 32 chemical reactions are included. Park's [13] two-temperature model is employed in order to take the thermal nonequilibrium state into account. The basic equations for the gasdynamics are written as follows.

Mass conservation equations of chemical species (s = N, O, N_2, O_2, NO, N^+, O^+, N_2^+, O_2^+, NO^+, e^-):

$$\frac{\partial \rho_s}{\partial t} + \frac{\partial}{\partial r}(\rho_s u_r) + \frac{\partial}{\partial z}(\rho_s u_z) = \dot{\omega}_s + \frac{\partial}{\partial r}\left(\rho D_s \frac{\partial y_s}{\partial r}\right) + \frac{\partial}{\partial z}\left(\rho D_s \frac{\partial y_s}{\partial z}\right) - \frac{1}{r}\left(\rho_s u_r - \rho D_s \frac{\partial y_s}{\partial r}\right) \tag{2}$$

where the total mass density ρ is given by

$$\rho = \sum_s \rho_s \tag{3}$$

The first term $\dot{\omega}_s$ on the right-hand side of Eq. (2) is the source term for the mass production rate of species s and is expressed as

$$\dot{\omega}_s = M_s \sum_{i=1}^{32} (\beta_{s,i} - \alpha_{s,i})(R_{f,i} - R_{b,i}) \tag{4}$$

The forward and backward reaction rates $R_{f,i}$ and $R_{b,i}$ are, respectively, defined by

$$R_{f,i} = k_{f,i} \prod_{s=1}^{11} (\rho_s / M_s)^{\alpha_{s,i}}, \qquad R_{b,i} = k_{b,i} \prod_{s=1}^{11} (\rho_s / M_s)^{\beta_{s,i}} \tag{5}$$

where the forward reaction rate coefficients $k_{f,i}$ and the backward reaction rate coefficients $k_{b,i}$ are tabulated in [12,14].

Momentum-conservation equations:

$$\frac{\partial \rho u_r}{\partial t}+\frac{\partial}{\partial r}(\rho u_r^2+p)+\frac{\partial}{\partial z}(\rho u_r u_z)=\frac{\partial \tau_{rr}}{\partial r}+\frac{\partial \tau_{rz}}{\partial z}+J_\theta B_z-\frac{1}{r}(\rho(u_r^2-u_\theta^2)-\tau_{rr}+\tau_{\theta\theta}) \tag{6}$$

$$\frac{\partial \rho u_\theta}{\partial t}+\frac{\partial}{\partial r}(\rho u_\theta u_r)+\frac{\partial}{\partial z}(\rho u_\theta u_z)=\frac{\partial \tau_{r\theta}}{\partial r}+\frac{\partial \tau_{z\theta}}{\partial z}+J_z B_r-J_r B_z-\frac{2}{r}(\rho u_r u_\theta-\tau_{r\theta}) \tag{7}$$

$$\frac{\partial \rho u_z}{\partial t}+\frac{\partial}{\partial r}(\rho u_z u_r)+\frac{\partial}{\partial z}(\rho u_z^2+p)=\frac{\partial \tau_{rz}}{\partial r}+\frac{\partial \tau_{zz}}{\partial z}-J_\theta B_r-\frac{1}{r}(\rho u_r u_z-\tau_{rz}) \tag{8}$$

where the static pressure p and the viscous stress terms $\tau_{i,j}$ are defined by

$$p=\sum_s p_s=\sum_{s=1-10}\rho_s\frac{\bar{R}}{M_s}T_{\mathrm{tr}}+\rho_e\frac{\bar{R}}{M_e}T_{\mathrm{ve}} \tag{9}$$

$$\tau_{rr}=\frac{2}{3}\mu\left(2\frac{\partial u_r}{\partial r}-\frac{\partial u_z}{\partial z}-\frac{u_r}{r}\right),\quad \tau_{\theta\theta}=\frac{2}{3}\mu\left(2\frac{u_r}{r}-\frac{\partial u_r}{\partial r}-\frac{\partial u_z}{\partial z}\right)$$
$$\tau_{zz}=\frac{2}{3}\mu\left(2\frac{\partial u_z}{\partial z}-\frac{\partial u_r}{\partial r}-\frac{u_r}{r}\right),\quad \tau_{r\theta}=\tau_{\theta r}=\mu\left(\frac{\partial u_\theta}{\partial r}-\frac{u_\theta}{r}\right) \tag{10}$$
$$\tau_{rz}=\tau_{zr}=\mu\left(\frac{\partial u_r}{\partial z}+\frac{\partial u_z}{\partial r}\right),\quad \tau_{\theta z}=\tau_{z\theta}=\mu\frac{\partial u_\theta}{\partial z}$$

Total-energy-conservation equation:

$$\begin{aligned}\frac{\partial \rho E}{\partial t}&+\frac{\partial}{\partial r}(\rho H u_r)+\frac{\partial}{\partial z}(\rho H u_z)=\frac{\partial}{\partial r}\left(\eta_{\mathrm{tr}}\frac{\partial T_{\mathrm{tr}}}{\partial r}+\eta_{\mathrm{ve}}\frac{\partial T_{\mathrm{ve}}}{\partial r}\right)\\&+\frac{\partial}{\partial z}\left(\eta_{\mathrm{tr}}\frac{\partial T_{\mathrm{tr}}}{\partial z}+\eta_{\mathrm{ve}}\frac{\partial T_{\mathrm{ve}}}{\partial z}\right)+\frac{\partial}{\partial r}\left(\rho\sum_s h_s D_s\frac{\partial y_s}{\partial r}\right)\\&+\frac{\partial}{\partial z}\left(\rho\sum_s h_s D_s\frac{\partial y_s}{\partial z}\right)+\frac{\partial}{\partial r}(\tau_{rr}u_r+\tau_{\theta r}u_\theta+\tau_{zr}u_z)\\&+\frac{\partial}{\partial z}(\tau_{rz}u_r+\tau_{\theta z}u_\theta+\tau_{zz}u_z)+J_rE_r+J_zE_z-\frac{\rho H u_r}{r}\\&+\frac{\rho}{r}\sum_s h_s D_s\frac{\partial y_s}{\partial r}+\frac{1}{r}\left(\eta_{\mathrm{tr}}\frac{\partial T_{\mathrm{tr}}}{\partial r}+\eta_{\mathrm{ve}}\frac{\partial T_{\mathrm{ve}}}{\partial r}\right)\\&+\frac{1}{r}(\tau_{rr}u_r+\tau_{\theta r}u_\theta+\tau_{zr}u_z)\end{aligned} \tag{11}$$

where the total enthalpy H is defined as

$$H=E+\frac{p}{\rho} \tag{12}$$

Vibrational-electronic-electron energy-conservation equation:

$$\begin{aligned}\frac{\partial \rho e_{\mathrm{ve}}}{\partial t}&+\frac{\partial}{\partial r}(\rho e_{\mathrm{ve}}u_r)+\frac{\partial}{\partial z}(\rho e_{\mathrm{ve}}u_z)=\dot{\omega}_{\mathrm{ve}}+\frac{\partial}{\partial r}\left(\eta_{\mathrm{ve}}\frac{\partial T_{\mathrm{ve}}}{\partial r}\right)\\&+\frac{\partial}{\partial z}\left(\eta_{\mathrm{ve}}\frac{\partial T_{\mathrm{ve}}}{\partial z}\right)+\frac{\partial}{\partial r}\left(\rho\sum_s h_{\mathrm{ve},s}D_s\frac{\partial y_s}{\partial r}\right)\\&+\frac{\partial}{\partial z}\left(\rho\sum_s h_{\mathrm{ve},s}D_s\frac{\partial y_s}{\partial z}\right)+\frac{J_r^2+J_\theta^2+J_z^2}{\sigma}\\&-\frac{1}{r}\left(\rho e_{\mathrm{ve}}u_r-\rho\sum_s h_{\mathrm{ve},s}D_s\frac{\partial y_s}{\partial r}-\eta_{\mathrm{ve}}\frac{\partial T_{\mathrm{ve}}}{\partial r}\right)\end{aligned} \tag{13}$$

where $\dot{\omega}_{\mathrm{ve}}$ is the source term for the production rate of vibrational-electronic-electron energy and is expressed as

$$\dot{\omega}_{\mathrm{ve}}=\sum_{s=\mathrm{mol}}\rho_s\frac{e^*_{v,s}-e_{v,s}}{<\tau_s>}+2\rho_e\frac{3}{2}\bar{R}(T_{\mathrm{tr}}-T_{\mathrm{ve}})\sum_{s\neq e}\frac{\nu_{e,s}}{M_s}-\sum_{s=\mathrm{ion}}\dot{n}_{e,s}I_s+\sum_{s=\mathrm{mol}}\dot{\omega}_s\hat{D}_s-p_e\left(\frac{\partial u_r}{\partial r}+\frac{\partial u_z}{\partial z}+\frac{u_r}{r}\right) \tag{14}$$

where the relaxation time τ_s of each species for a translational-vibrational energy relaxation is calculated from the sum of the relaxation time formula proposed by Millikan and White [15] and the correction term suggested by Park [13]. The effective energy exchange frequency ν_{es} of electrons with other species is estimated by following [14]. The average vibrational energy $\hat{D}_s$, which is created or destroyed at the rate $\dot{\omega}_s$, is computed by using the nonpreferential model [14].

The transport coefficients such as the effective diffusion coefficient D_s of each species, the mixture viscosity μ, the mixture translational-rotational thermal conductivity η_{tr}, and the mixture vibrational-electron thermal conductivity η_{ve} are estimated by an extension model of Yos's formulas to the multitemperature gas mixture (see [14]).

The basic equations for the electrodynamics are the steady Maxwell equations and the generalized Ohm's law. The present study neglects the induced magnetic field because the electrodynamics in the shock layer are dominated by the Hall effect and the magnetic Reynolds number R_m, estimated by using the effective electrical conductivity $\sigma/(1+\beta^2)$ with the consideration of the Hall effect, is less than unity ($R_m<0.01$) under the present numerical condition. The basic equations for the electrodynamics are written as follows.

Maxwell equations:

$$\nabla\times\boldsymbol{E}=0 \tag{15}$$

$$\nabla\cdot\boldsymbol{J}=0 \tag{16}$$

Generalized Ohm's law:

$$\begin{pmatrix}J_r\\J_\theta\\J_z\end{pmatrix}=\frac{\sigma}{1+\beta^2}\begin{pmatrix}1+m^2B_r^2 & -mB_z & m^2B_rB_z\\ mB_z & 1 & -mB_r\\ m^2B_rB_z & mB_r & 1+m^2B_z^2\end{pmatrix}\begin{pmatrix}E_r+u_\theta B_z+\frac{1}{en_e}\frac{\partial p_e}{\partial r}\\ u_zB_r-u_rB_z\\ E_z-u_\theta B_r+\frac{1}{en_e}\frac{\partial p_e}{\partial z}\end{pmatrix}\qquad m=\beta/|\boldsymbol{B}| \tag{17}$$

The electrical conductivity σ and the Hall parameter β are, respectively, expressed as

$$\sigma=\frac{n_e e^2}{m_e\sum_{s\neq e}\nu^m_{e,s}},\qquad \beta=\frac{e|\boldsymbol{B}|}{m_e\sum_{s\neq e}\nu^m_{e,s}} \tag{18}$$

The effective momentum transfer collision frequency $\nu^m_{e,s}$ of electrons with the other chemical species s is written as

$$\nu^m_{e,s} = \begin{cases} 6\pi\left(\frac{e^2}{12\pi\epsilon_0 k_b T_{\rm ve}}\right)^2 \ell_n\left[12\pi\left(\frac{\epsilon_0 k_b}{e^2}\right)^{3/2}\sqrt{\frac{T^3_{\rm ve}}{n_e}}\right] n_s\sqrt{\frac{8k_bT_{\rm ve}}{\pi m_e}} & \text{if } s \text{ is ion species} \\ \frac{4}{3}\sigma^m_{e,s} n_s\sqrt{\frac{8k_bT_{\rm ve}}{\pi m_e}} & \text{otherwise} \end{cases} \tag{19}$$

where the effective collision cross section of electrons with the other neutral chemical species s $\sigma_{e,s}$ is computed using the curve fit presented in [14]; the curve fit was generated from the effective collision cross-sectional data in [16]. Under the present flight conditions, the vibrational-electronic-electron temperature $T_{\rm ve}$ and the overall effective transfer collision frequencies of electrons

$$\sum_{s\neq e}\nu^m_{e,s}$$

in the shock layer are 7000 to 8000 K and the order of magnitude of 10^9 1/s, respectively. The collision frequency of electrons with N_2, which has the order of magnitude of 10^9 1/s, most contributes to the overall effective transfer collision frequencies of electrons, followed by the collision frequency of electrons with NO^+, which has the order of magnitude of 10^8 1/s.

D. Numerical Procedure

A computational region and a computational grid (normal grid) are illustrated in Fig. 6. The number of grid points is 65 in the ξ direction along the wall surface and 250 in the outward η direction. Because the prediction of the wall heat flux is extremely sensitive to the mesh size near the wall surface, the dependence of the wall heat flux on the mesh size near the wall surface was checked in advance. Based on the check, we set the minimum mesh size near the wall surface to about 2 μm. Furthermore, the authors checked the dependence of the generator performance on grids under the maximum electrical output power conditions ($B_0 = 0.5$ T and $V_L = 2930$ V). For this check, the grid point in the η direction in the shock layer was changed. The computed electrical output power had a slightly decrease tendency for the increase of the grid point in the η direction. The difference of electric output power between a coarse grid ($\xi 65 \times \eta 170$) and the normal grid ($\xi 65 \times \eta 250$) was about 2.3% of the electrical output power in the normal grid. Its difference between a fine grid ($\xi 65 \times \eta 350$) and the normal grid ($\xi 65 \times \eta 250$) was about 0.5% of the electrical output power in the normal grid. The electrical output power between the fine grid and the normal grid has no influence on the discussion in the present paper. The normal grid illustrated in Fig. 6 was therefore employed in the present study.

The conservation equations of the gasdynamics are transformed into the generalized coordinate system. The convection terms are calculated by the advection upstream splitting method AUSM-DV [17] coupled with the second-order MUSCL total-variation-diminishing scheme. The viscous terms are calculated by the second-order central-differencing scheme. The time integration is performed by the lower/upper symmetric Gauss–Seidel scheme [18]. The boundary conditions for the gasdynamics are specified as follows.

For inflow (the boundary line B_1 in Fig. 6), the freestream conditions are given as

$$\frac{\rho_{N_2}}{\rho} = 0.79, \qquad \frac{\rho_{O_2}}{\rho} = 0.21, \qquad u_z = U_\infty, \qquad u_r = u_\theta = 0$$

$$p = P_\infty, \qquad T_{\rm tr} = T_{\rm ve} = T_\infty$$

For outflow (the boundary line B_2 in Fig. 6), the gradients of all primitive variables (ρ_s, u_z, u_r, u_θ, $T_{\rm tr}$, and $T_{\rm ve}$) in the ξ direction are set to zero. For symmetric lines (the boundary line B_3 in Fig. 6), u_r and u_θ are set to zero, and the normal gradient is set to zero for the other primitive variables (ρ_s, u_z, $T_{\rm tr}$, and $T_{\rm ve}$). For the wall surface (the boundary line B_4 in Fig. 6), the no-slip condition, the fixed-wall-temperature condition, and the noncatalytic wall condition are used, and the translational-rotational temperature $T_{\rm tr}$ and the vibrational-electron temperature $T_{\rm ve}$ on the wall surface are assumed to be in equilibrium with the wall temperature T_W. The wall temperature T_W is set to 1519 K; this value corresponds to the wall temperature at the stagnation point estimated at the altitude of about 60 km in the OREX experiments.

We derive a second-order partial differential equation on the electric potential from Eqs. (15–17). The equation is solved by the Galerkin finite element method. The boundary conditions in the case with extracting electric power are as follows:

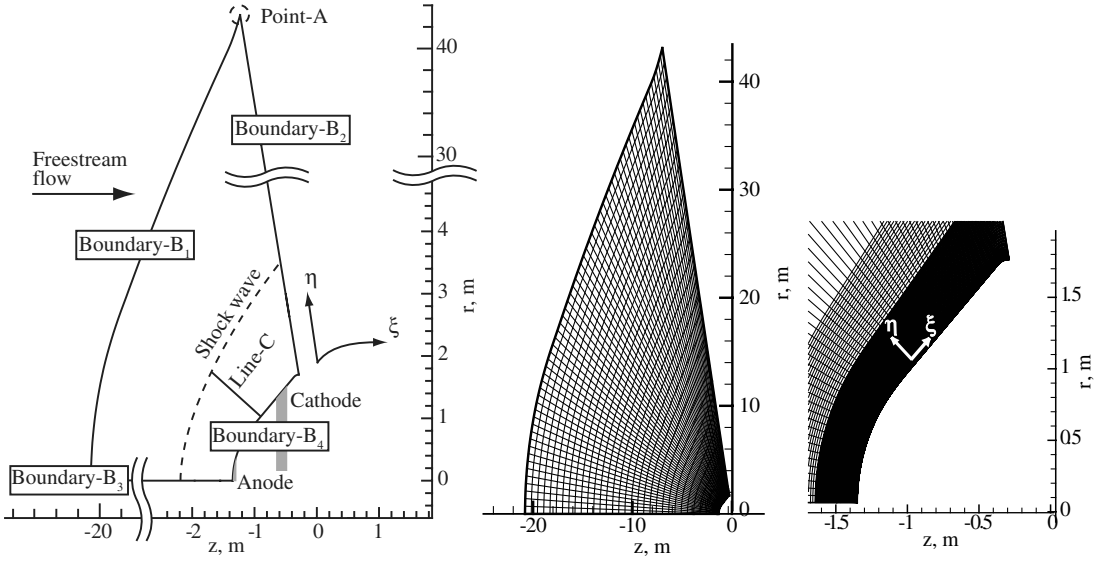

Fig. 6 Computational region and computational grid.

1) For inflow (the boundary line B_1 in Fig. 6), outflow (the boundary line B_2 in Fig. 6), the symmetric line (the boundary line B_3 in Fig. 6), and the wall surface (the boundary line B_4 in Fig. 6), the normal component of electric current density on the boundary lines is set to 0 A/m^2.

2) For the anode electrode, the electric potential ϕ_{anode} on the anode electrode is set to 0 V.

3) For the cathode electrode, the electric potential $\phi_{cathode}$ on the cathode electrode, that is, the load voltage V_L is given as

$$\phi_{cathode} = V_L = R_{ext} \cdot I$$

where the load current I is obtained by computing the surface integral of the electric current density perpendicular to the line C in Fig. 6.

The present study also conducts the numerical simulation in the case without electrodes: that is, in the case without extracting electric power. The boundary conditions in the case without electrodes are as follows: the normal component of electric current density is set to 0 A/m^2 on all boundary lines in Fig. 6, and the electric potential ϕ at the point A in Fig. 6 is set to 0 V for establishing a reference value of electric potential.

Power-generation experiments using a test body with Hall-type MHD power generation proposed in the present study have not yet been conducted under a ground hypersonic-tunnel environment or a real reentry-fight environment. The part of gasdynamics including thermochemical-reaction models and the part of electrodynamics in the developed computational code were therefore validated separately. As shown in [19], we compared the shock location of both numerical results and experimental data in Lobb's experiments [20] to validate the reliability of the numerical solutions for the gasdynamics part including thermochemical reactions. As a result, good agreement between numerical results and experimental data was obtained. The electrodynamics part in the developed computational code has been widely used for many years in our numerical studies (for example, [21,22]) on MHD power generators such as a large-scale Faraday-type MHD generator (Sakhalin) with the electrical output power of 510 MW [21] and a shock-tube-driven Hall-type MHD power generator in the Tokyo Institute of Technology with high generator efficiency [22]. These numerical studies have clearly shown that the reliability of the numerical solutions for the electrodynamics part is very high.

III. Results and Discussion

Figure 7 illustrates the relationships between the electrical power and the load voltage for the parameter $B_0 = 0.3$, 0.4, and 0.5 T. This figure demonstrates that the onboard surface Hall-type MHD power generator shown in Fig. 4, at least in principle, can extract the electrical power above 1 MW by applying the magnetic field with the strength of 0.3–0.5 T. The electric power can be also controlled over a wide range (from a few hundred kilowatts to a few megawatts) by adjusting the load voltage and the strength of the applied magnetic field, as shown in Fig. 7.

In the following, influences of the load voltage on the electrodynamics, the gasdynamics, and the wall heat flux are first discussed, mainly from numerical results under the applied magnetic field condition of the parameter $B_0 = 0.5T$, and then influences of the strength of the applied magnetic field are discussed briefly.

As can be found from Fig. 7, there is an optimum load voltage to maximize the electrical power for any value of the parameter B_0. The optimum load voltage for the parameter $B_0 = 0.5$ T is 2930 V, and the electrical power and the load current for the optimum load voltage are about 2.87 MW and about 980 A, respectively. In the low-load-voltage part below the optimum load voltage, the electrical power increases with the load voltage. Although there are few data in the high-load-voltage part above the optimum load voltage for any value of the parameter B_0 because of the divergence of numerical solutions, the electrical power in the high-load-voltage part is on a declining trend for the increase of load voltage. The reason of the divergence of numerical solutions in the high-load-voltage part is not entirely clear at the moment, but we suppose that it is one of possible reasons that the closed path of electric current comes to be formulated in the shock layer in the high-load-voltage part because of large impedance mismatching between the plasma and the external load, and so the electric current cannot flow between the electrodes.

As mentioned in the Numerical Methods and Numerical Conditions section, the electrical power in Fig. 7 was computed under the wall temperature T_W of 1519 K. The authors checked a sensibility of the electrical power to the wall temperature by changing it in a range of 1000 to 2000 K under the optimum load voltage for the parameter $B_0 = 0.5$ T. The electrical output power slightly decreased with the increase of the wall temperature for the optimum load-voltage condition, but the difference of the electrical output power between $T_W = 1000$ and 2000 K is about 15 kW and very small.

Figure 8 depicts relationships between the load voltage and the load current for the parameter $B_0 = 0.3$, 0.4, and 0.5 T. For any value of the parameter B_0, the load current becomes larger with decreasing load voltage.

As shown in Fig. 9, the increase of the thickness of the shock layer by applying the magnetic field becomes more pronounced with the increase of the load voltage. However, the effect of the applied magnetic field on the increase of the thickness of the shock layer for any load voltage in the case with extracting electrical power is significantly weaker than that in the case without electrodes. Furthermore, in the case with extracting electrical power, the shock standoff distance ahead of the anode electrode is not much affected by applying the magnetic field for any load voltage.

Figure 10 shows two-dimensional distributions of electrical conductivity and ionization degree for the load voltage of $V_L = 2931$ V. The maximum electrical conductivity and maximum

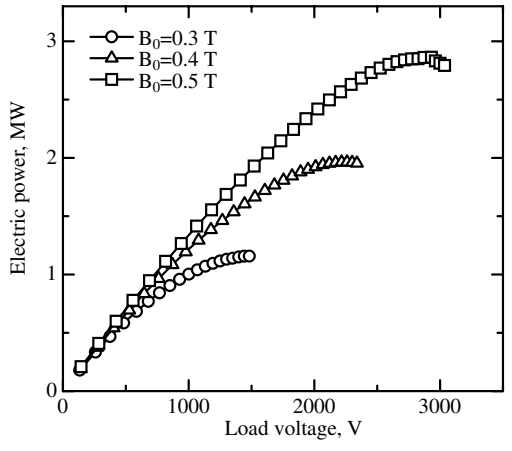

Fig. 7 Relationships between electrical power and load voltage for the parameter $B_0 = 0.3$, 0.4, and 0.5 T.

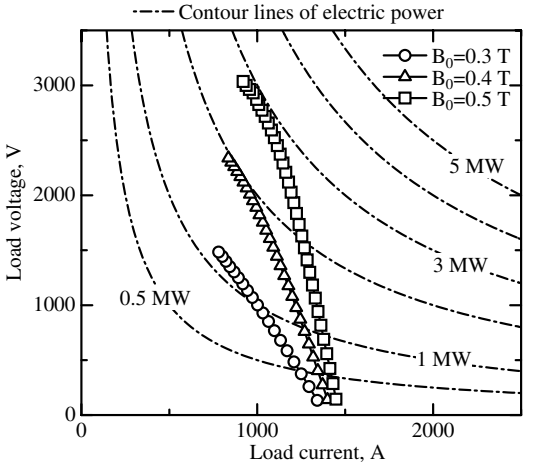

Fig. 8 Relationships between load voltage and load current for the parameter $B_0 = 0.3$, 0.4, and 0.5 T.

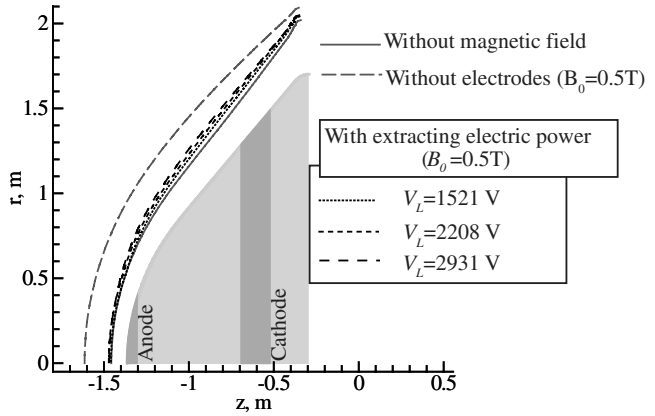

Fig. 9 Positions of shock waves in the case without magnetic field ($B_0 = 0.0$ T), in the case without electrodes ($B_0 = 0.5$ T), and in the cases with extracting electric power under some load-voltage conditions ($B_0 = 0.5$ T.

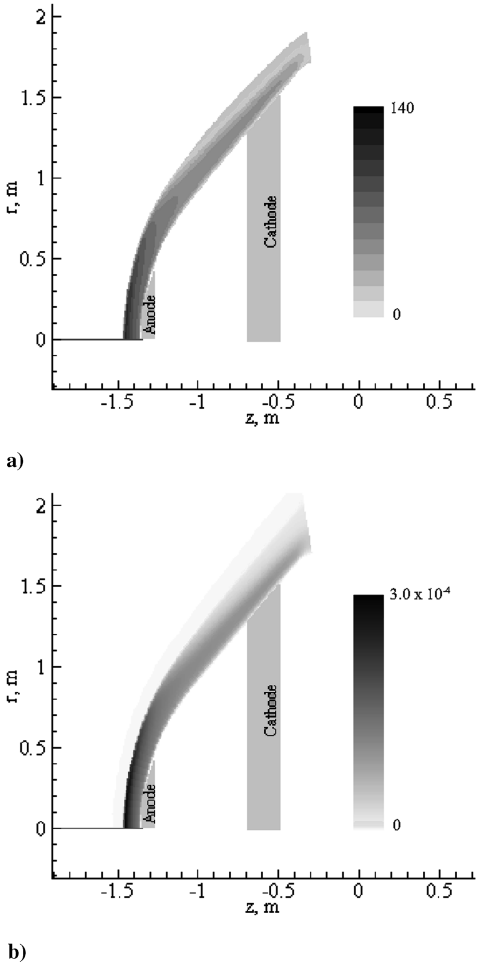

Fig. 10 Two-dimensional distributions of a) electrical conductivity and b) ionization degree for the load voltage of $V_L = 2931$ V. The parameter B_0 is 0.5 T.

ionization degree in the shock layer have about 120 S/m and about 3×10^{-4}, respectively. Figure 11 illustrates distributions of electrical conductivity and the Hall parameter along the stagnation line in the four cases: load voltage $V_L = 1521$, 2208, and 2931 V and without electrodes. The load-voltage condition has little influence on the values of the electrical conductivity and the Hall parameter in the shock layer, and the maximum values of the electrical conductivity and the Hall parameter in the shock layer for any load voltage are

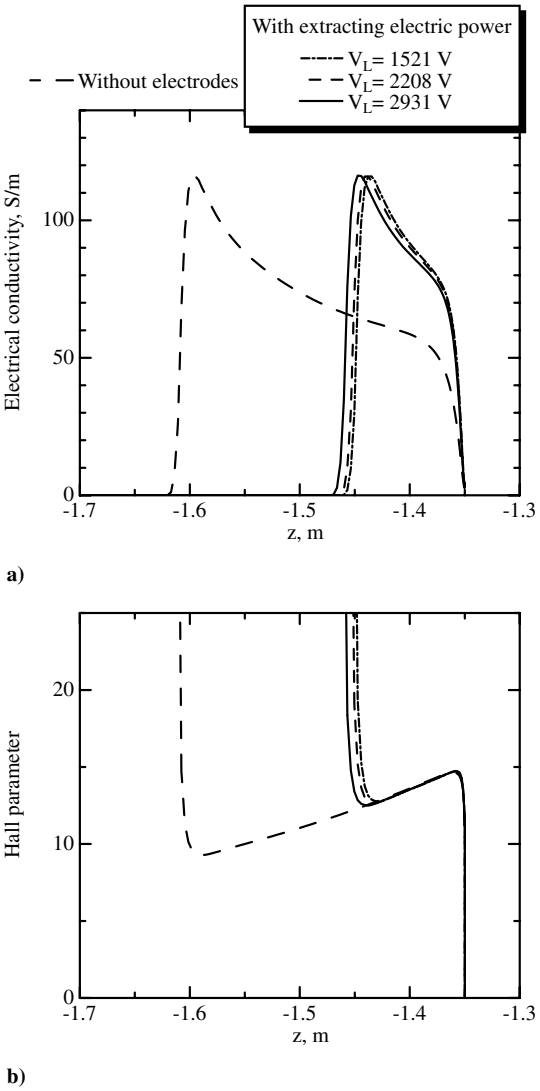

Fig. 11 Distributions of a) electrical conductivity and b) Hall parameter along the stagnation line in the four cases: load voltage $V_L = 1521$, 2208, and 2931 V, and without electrodes. The parameter B_0 is 0.5 T for all cases.

almost the same as those in the case without electrodes: that is, without extracting electrical power. The maximum values of the electrical conductivity and the Hall parameter in the shock layer are about 120 S/m and about 18, respectively, for any load voltage. The large Hall parameter indicates that the electrodynamics in the shock layer is dominated by the Hall effect.

The Lorentz force, which is induced by the interaction between the positive azimuthal θ electric current density and the applied magnetic field with the r and z components, decelerates the weakly ionized plasma flow in the shock layer, and so the thickness of the shock layer is increased. As shown in Fig. 12, the azimuthal electric current density in the case with extracting electrical power becomes larger with increasing load voltage. This fact results in the effect of the applied magnetic field on the increase of the thickness of the shock layer being more clearly seen as the load voltage increases. For any load voltage in the case with extracting electrical power, however, the azimuthal electric current density ahead of the anode electrode is vanishingly small, and so the shock standoff distance ahead of the anode electrode is not much affected by applying the magnetic field for any load voltage.

It can be also found from Fig. 12 that the large azimuthal electric current density can be obtained in a wider region in the case without electrodes than in the cases with extracting electrical power. As a result, the increase of the thickness of the shock layer by applying the magnetic field is seen more clearly in the case without electrodes than

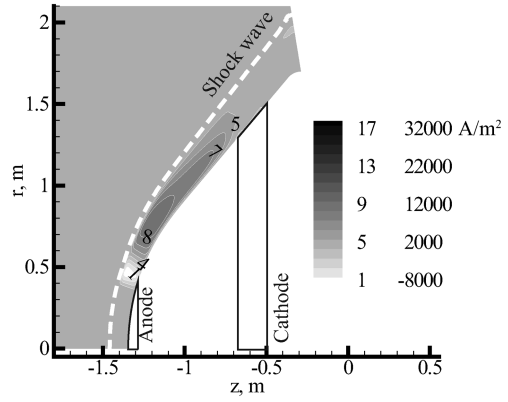

a) V_L=1521 V

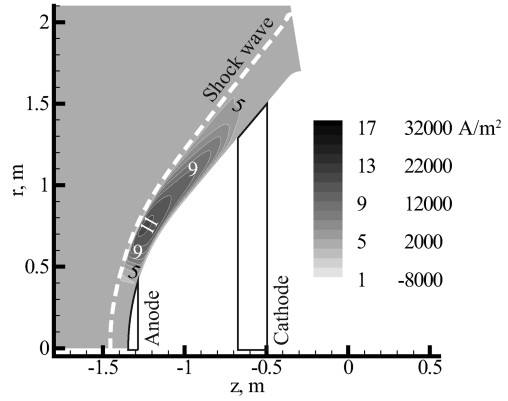

b) V_L=2208 V

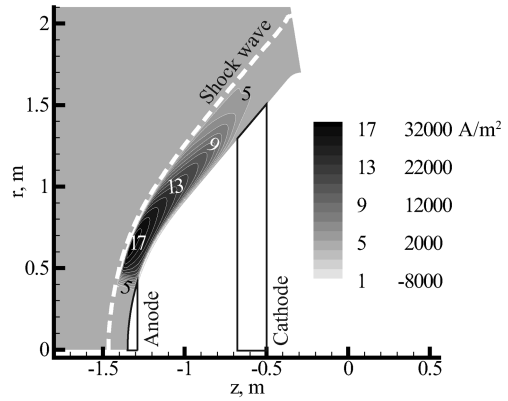

c) V_L=2931 V

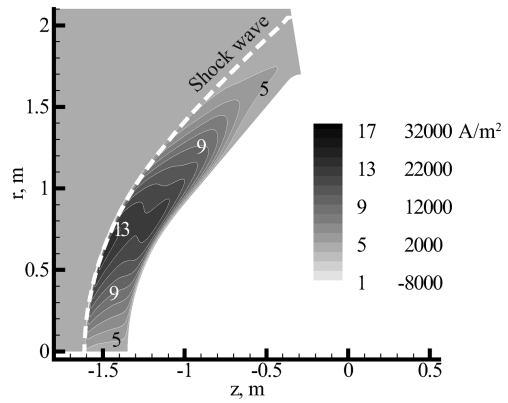

d) Without electrodes

Fig. 12 Distributions of azimuthal electric current density J_θ in the four cases the load voltage. The parameter B_0 is 0.5 T for all cases.

in the case of extracting electrical power. It should be also noted in Fig. 12 that the region in which the sign of the azimuthal electric current density is negative exists near the anode edge for the load voltage of $V_L = 1521$ V. The region with the negative azimuthal electric current density becomes wider with decreasing load voltage. The Lorentz force induced by the interaction between the negative azimuthal electric current density and the applied magnetic field gives rise to the acceleration of the flow in the shock layer. The acceleration of the flow in the shock layer drives the bow shock wave closer to the body. The existence of the region with the negative azimuthal electric current density is therefore undesirable from the standpoint of the MHD thermal protection aiming at the reduction of the wall heat flux.

When the Hall effect dominates the electrodynamics, the magnitude of azimuthal electric current density strongly depends on the strength of the Hall electric field induced on the r–z plane. The stronger the component of the Hall electric field in the direction from the cathode to the anode becomes, the larger the positive azimuthal electric current density. Figure 13 illustrates two-dimensional (r–z) distributions of the electric potential under some load-voltage conditions for the parameter $B_0 = 0.5$ T. One-dimensional distributions of the electric potential on the wall surface under various load-voltage conditions are illustrated in Fig. 14. It can be found from Figs. 13 and 14 that the component of the Hall electric field in the direction from the cathode to the anode, which is called the *positive Hall electric field* here, becomes stronger in the shock layer with increasing load voltage. This result leads to the azimuthal electric current density increasing with the load voltage, and so the increase of the thickness of the shock layer by applying the magnetic field is seen more clearly with the increase of the load voltage.

We can also find from Figs. 13 and 14 that the component of the Hall electric field in the direction from the anode to the cathode, which is called the *negative Hall electric field* here, appears near the anode edge under the low-load-voltage conditions. The negative Hall electric field induces the negative azimuthal electric current density near the anode edge. The negative Hall electric field disappears with the increase of the load voltage. This is because the increase of the load voltage decreases the load current, and so the voltage loss attributed to the internal resistance decreases with the increase of the load voltage. Furthermore, it can be seen from Fig. 13 that the Hall electric field ahead of the anode with the constant electric potential ($\phi = 0$ V) is almost zero for any load voltage. This prohibits large azimuthal electric current density from forming ahead of the anode for any load voltage, as shown in Fig. 12. As a result, the shock standoff distance ahead of the anode cannot be increased by applying the magnetic field for any load voltage, as shown in Fig. 9.

We can find from the comparison of Figs. 2 and 13 that in the case without electrodes, which corresponds to an electrically open circuit condition, the large positive Hall electric field can be obtained in a wider region than in the cases with extracting electrical power, and so the large positive azimuthal electric current density can be obtained in a wider region in the case without electrodes than in the cases with extracting electrical power.

As shown in Fig. 15, the wall heat flux decreases with the increase of the load voltage, because the effect of the applied magnetic field on the increase of the thickness of the shock layer becomes stronger with the increase of the load voltage. Under the low-load-voltage conditions, however, the wall heat flux near the anode edge is larger than that in the case without applying the magnetic field. This is because the load current constricts on the anode edge, as shown in Fig. 16, and the magnitude of its constriction becomes larger with the decrease of the load voltage, because the load current increases with the decrease of the load voltage, as depicted in Fig. 8.

It can be also found from Fig. 15 that the effect of the applied magnetic field on the reduction of wall heat flux for any load voltage in the case with extracting electrical power is weaker than that in the case without electrodes. This is because the effect of the applied magnetic field on the increase of the thickness of the shock layer for any load voltage in the case with extracting electrical power is weaker than that in the case without electrodes. However, we predict that the effect of the applied magnetic field on the increase of the

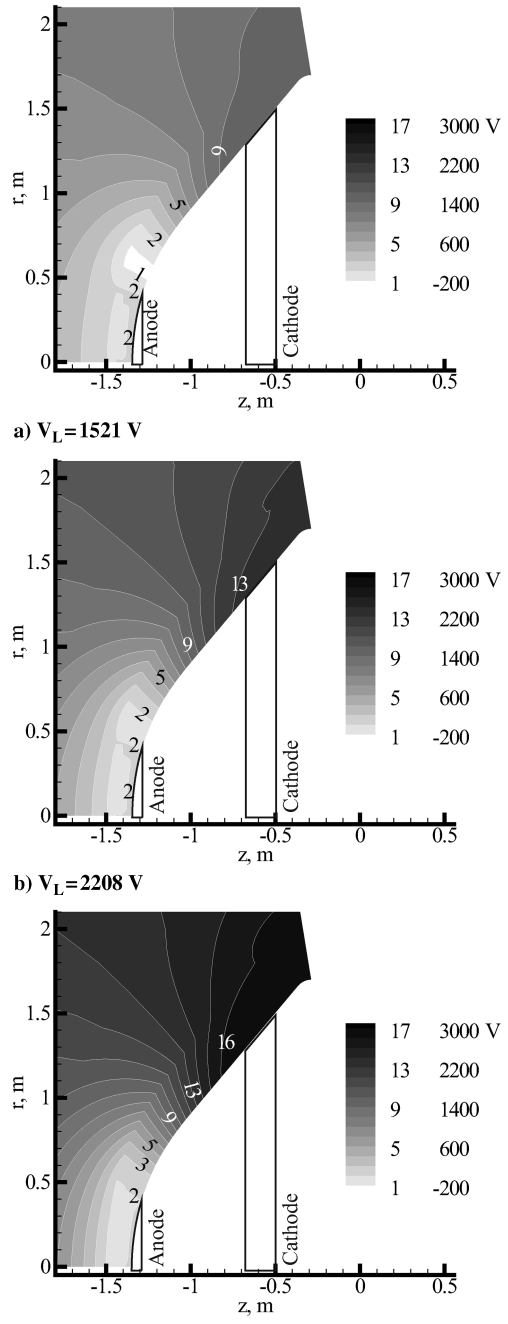

Fig. 13 Two-dimensional (r–z) distributions of electric potential in the three cases. The parameter B_0 is 0.5 T for all cases.

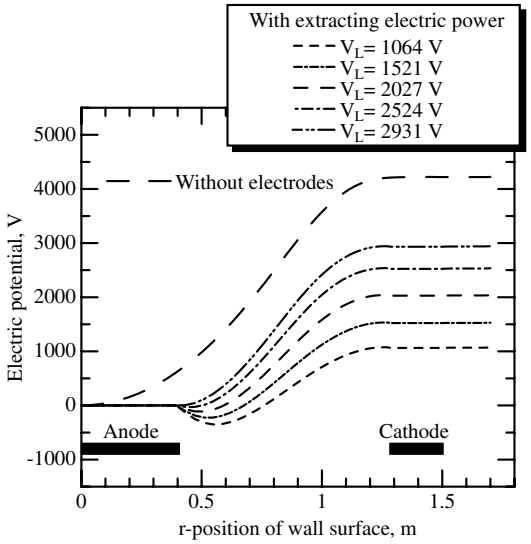

Fig. 14 Distributions of electric potential on wall surface in the cases with extracting electric power under various load-voltage V_L conditions, and its distribution in the case without electrodes. The parameter B_0 is 0.5 T for all cases.

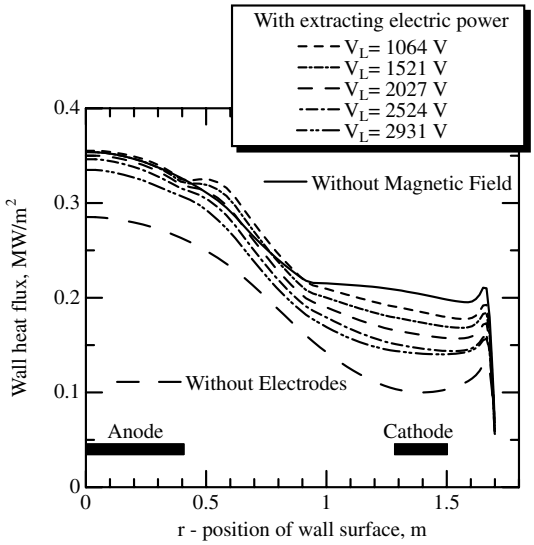

Fig. 15 Distributions of wall heat flux in the cases with extracting electric power under various load-voltage conditions V_L ($B_0 = 0.5$ T), its distribution in the case without electrodes ($B_0 = 0.5$ T), and its distribution in the case without magnetic field ($B_0 = 0.0$ T).

thickness of the shock layer in the cases with extracting electrical power can be strengthened by shortening the width of the anode, because the region in which the Hall electric field is almost zero is expected to become narrower.

As reported in [23,24], the MHD interaction in the shock layer provides an additional drag of a body. The drag attributed to the MHD interaction is about 7% of the pressure drag under the optimum load-voltage condition for the parameter $B_0 = 0.5$ T, and so the MHD drag has little impact on the total drag. However, we predict that the influence of the MHD on the total drag becomes stronger at higher flight altitude conditions, because the increase of the flight altitude leads to the decrease of the pressure drag and to the increase of the electrical conductivity.

In the following, we briefly discuss the influences of the strength of the applied magnetic field. It can be found from Fig. 7 that the maximum electrical power increases with the strength of the applied magnetic field, and the optimum load voltage at which the electric power takes the maximum value becomes higher with the increase of the strength of the applied magnetic field.

Figure 17 depicts distributions of the wall heat flux for each optimum load voltage in the three cases of the parameter $B_0 = 0.3$, 0.4, and 0.5 T. The wall heat flux in the case without applying magnetic field is also shown in Fig. 16. It can be found from Fig. 16 that the increase of the strength of the applied magnetic field results in the reduction of wall heat flux.

Figure 18 illustrates distributions of the flow velocity $\sqrt{u_r^2 + u_z^2}$ and the Hall parameter along one line in the η direction ($\xi = 20$) for each optimum load voltage in the three cases of the parameter $B_0 = 0.3$, 0.4, and 0.5 T. Figure 18a shows that the flow velocity in the shock layer decreases and the shock standoff distance increases as the strength of the applied magnetic field increases. It can be also found from Fig. 18b that the Hall parameter in the shock layer approximately linearly increases with the strength of the applied magnetic field. Both the increase of the strength of the applied magnetic field and the increase of the Hall parameter contribute to the

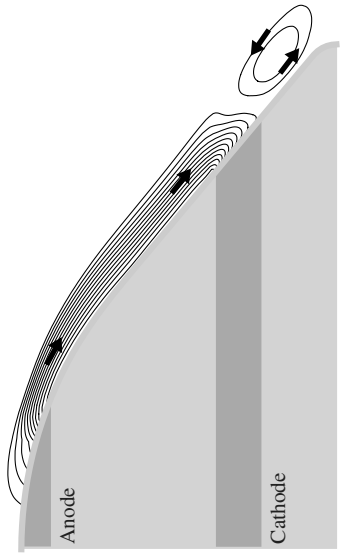

Fig. 16 Streamlines of electric current on the r–z plane for the load voltage $V_L = 145$ V and the parameter $B_0 = 0.5$ T, where the load current has a maximum value in the present numerical simulation.

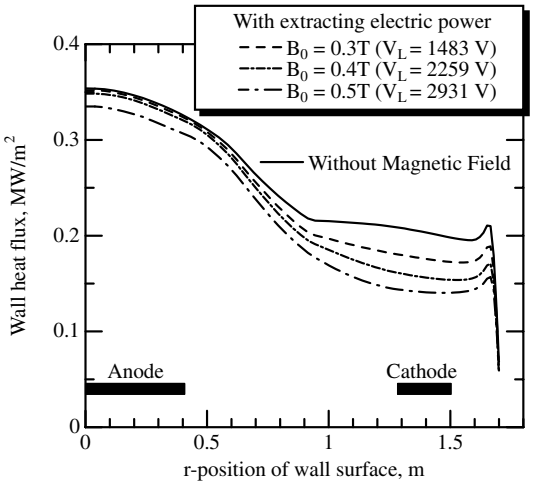

Fig. 17 Distributions of wall heat flux for each optimum load voltage in the three cases of the parameter $B_0 = 0.3$, 0.4, and 0.5 T, and its distribution without magnetic field ($B_0 = 0.0$ T).

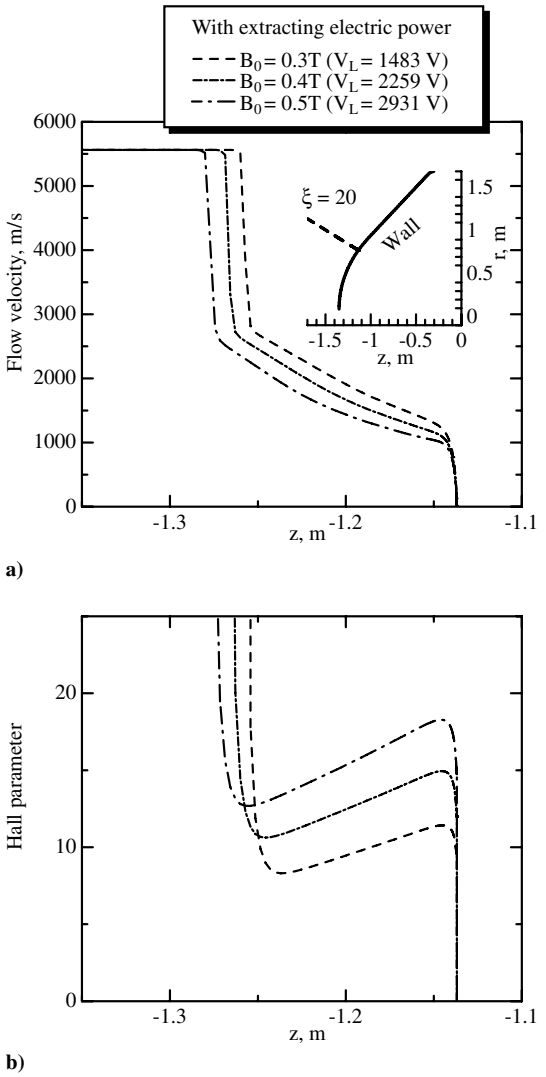

Fig. 18 Distributions of a) flow velocity and b) Hall parameter along one line in the η direction ($\xi = 20$) for each optimum load voltage in the three cases of the parameter $B_0 = 0.3$, 0.4, and 0.5 T.

increase of the Hall electromotive force (that is, to the increase of the Hall electric field), and so the azimuthal electric current density becomes larger with the increase of the strength of the applied magnetic field. The MHD interaction therefore becomes stronger with the increase of the strength of the applied magnetic field. As a result, the electric power increases, the flow velocity decreases, and the wall heat flux reduces with the increase of the strength of the applied magnetic field. The increase of the strength of the applied magnetic field also leads to the elevation of the open voltage between electrodes, because the Hall electric field becomes stronger with the increase of the strength of the applied magnetic field. The optimum load voltage therefore increases with the strength of the applied magnetic field.

IV. Conclusions

The feasibility of the electrical power extraction during Earth-reentry flights by using the onboard surface Hall-type MHD power generator has been numerically examined by using an axisymmetric two-dimensional computational fluid dynamics code, which accounts for the thermochemical nonequilibrium states and the Hall effect. Moreover, the present study has numerically explored the influence of the applied magnetic field on the wall heat flux when the electrical power is extracted by the onboard surface Hall-type MHD power generator. The present study has assumed that the reentry body with a nose radius of 1.35 m is equipped with a pair of electrodes on the wall surface for constructing onboard surface Hall-type MHD power generation. The present numerical simulation has been conducted under the following flight condition: the flight velocity is about 5.6 km/s and the flight altitude is about 60 km. The strength of the applied magnetic field has been varied in a range of about 0.3 to 0.5 T. The results are summarized as follows.

1) The present study has demonstrated by numerical simulation that it is possible to extract electrical power in excess of 1 MW with the onboard surface Hall-type MHD power generator by applying the magnetic field of 0.3–0.5 T at the altitude of about 60 km and the flight velocity of about 5.6 km/s. The output power can be controlled over a wide range (from a few hundred kilowatts to a few megawatts) by adjusting the load voltage and the strength of the applied magnetic field.

2) The effects of the applied magnetic field on the increase of the thickness of the shock layer and the reduction of the wall heat flux becomes stronger with the increases of the load voltage and the strength of the applied magnetic field, because those increases result in the strengthening of the MHD interaction. However, the effect of the applied magnetic field on the increase of the thickness of the shock layer and the reduction of the wall heat flux in the case with extracting electrical power is significantly weaker than in the case

without electrodes: that is, the case without extracting electrical power. This is mainly because the Hall electric field in the region ahead of the anode electrode becomes almost zero in the case with extracting electrical power, and so the region in which the strong MHD interaction can be obtained is much narrower in the case with extracting electrical power than in the case without electrodes.

The present numerical simulation has been conducted under only one reentry-flight condition. We can easily predict that the generator performance of the onboard surface Hall-type MHD power generator strongly depends on the reentry-flight conditions, because the plasma parameters such as the electrical conductivity and the Hall parameter strongly depend on reentry-flight conditions. Influences of the reentry-flight conditions on the generator performance will therefore be examined in our near-future study. We will also numerically examine the influences of the configuration of electrodes on the generator performance and the reduction of the wall heat flux by MHD effects in our near-future study.

Acknowledgments

This study was partly supported by University of Tsukuba Research Project. A part of computation in the present study was performed with the KDK system of Research Institute for Sustainable Humanosphere (RISH) at Kyoto University.

References

[1] Meyer, R. C., "On Reducing Aerodynamic Heat-Transfer Rates by Magnetohydrodynamic Techniques," *Journal of the Aero/Space Sciences*, Vol. 25, No. 9, 1958, pp. 561–566, 572.

[2] Bush, W. B., "*Magnetohydrodynamic-Hypersonic Flow Past a Blunt Body*," *Journal of the Aero/Space Sciences*, Vol. 25, No. 11, 1958, pp. 685–690, 728.

[3] Ziemer, R. W., "Experimental Investigation in Magneto-Aerodynamics," *ARS Journal*, Vol. 29, No. 19, 1959, pp. 642–647.

[4] Fujino, T., and Ishikawa, M., "Numerical Simulation of Control of Plasma Flow with Magnetic Field for Thermal Protection in Earth Reentry Flight," *IEEE Transactions on Plasma Science*, Vol. 34, No. 2, 2006, pp. 409–420.
doi:10.1109/TPS.2006.872458

[5] Fujino, T., Funaki, I., Sugita, H., Mizuno, M., and Ishikawa, M., "Influences of Electrical Conductivity of Wall on Magnetohydrodynamic Control of Aerodynamic Heating," *Journal of Spacecraft and Rockets*, Vol. 43, No. 1, 2006, pp. 63–70.
doi:10.2514/1.13770

[6] Fujino, T., and Ishikawa, M., "Numerical Studies of Magnetohydrodynamic Flow Control Considering Real Wall Electrical Conductivity," *Journal of Spacecraft and Rockets*, Vol. 44, No. 3, 2007, pp. 625–632.
doi:10.2514/1.25824

[7] Yamamoto, Y., "Recent Comparisons of Aerothermodynamic Results by CFD and FEM Coupling Analysis with OREX Flight Experiments," *Proceedings of the 13th NAL Symposium on Aircraft Computational Aerodynamics*, National Aerospace Lab. of Japan, Tokyo, 1995, pp. 27–39.

[8] Bityurin, V. A., Zeigarnik, V. A., and Kuranov, A. L., "On a Perspective of MHD Technology in Aerospace Applications," AIAA Paper 1996–2355, June 1996.

[9] Macheret, S. O., Shneider, M. N., and Candler, G. V., "Modeling of MHD Power Generation on Board Reentry Vehicles," AIAA Paper 2004–1024, Jan. 2004.

[10] Wan, T., Gandler, G. V., Macheret, S. O., Shneider, M. N., and Miles, R. B., "CFD Modeling and Simulations of MHD Power Generation During Re-Entry," AIAA Paper 2004–2562, June 2004.

[11] Wan, T., Suzuki, R., Gandler, G. V., Macheret, S. O., and Shneider, M. N., "Three Dimensional Simulation of Electric Field and MHD Power Generation During Re-Entry," AIAA Paper 2005–5045, June 2005.

[12] Kang, S. W., Jones, W. L., and Dunn, M. G., "Theoretical and Measured Electron-Density Distributions at High Altitudes," *AIAA Journal*, Vol. 11, No. 2, 1973, pp. 141–149.
doi:10.2514/3.50446

[13] Park, C., "Assessment of Two-Temperature Kinetic Model for Ionizing Air," *Journal of Thermophysics and Heat Transfer*, Vol. 3, No. 3, 1989, pp. 233–244.
doi:10.2514/3.28771

[14] Gnoffo, P. A., Gupta, R. N., and Shinn, J. L., "Conservation Equations and Physical Models for Hypersonic Air Flows in Thermal and Chemical Nonequilibrium," NASA TP–2867, Feb. 1989.

[15] Millikan, R. C., and White, D. R., "Systematics of Vibrational Relaxation," *Journal of Chemical Physics*, Vol. 39, No. 12, 1963, pp. 3209–3213.
doi:10.1063/1.1734182

[16] Gupta, R. N., Yos, J. M., Thompson, R. A., and Lee, K. P., "A Review of Reaction Rates and Thermodynamic and Transport Properties for an 11-Species Air Model for Chemical and Thermal Nonequilibrium Calculations to 30,000 K," NASA RP–1232, Aug. 1990.

[17] Wada, Y., and Liou., M-S., "A Flux-Splitting Scheme with High-Resolution and Robustness for Discontinuities," AIAA Paper 94–0083, Jan. 1994.

[18] Yoon, S., and Jameson, A., "Lower-Upper Symmetric-Gauss-Seidel Method for the Euler and Navier-Stokes Equations," *AIAA Journal*, Vol. 26, No. 9, 1988, pp. 1025–1026.
doi:10.2514/3.10007

[19] Fujino, T., Funaki, I., Sugita, H., Mizuno, M., and Ishikawa, M., "Numerical Analyses on Flow Control Around Blunt Body 'OREX' by Magnetic Field," AIAA Paper 2003–3760, June 2003.

[20] Lobb, R. K., "Experimental Measurement of Shock Detachment Distance on Spheres Fired in Air at Hypervelocities," *The High Temperature Aspects of Hypersonic Flow*, edited by W. C. Nelson, Pergamon, New York, 1964, pp. 519–527.

[21] Yuhara, M., and Fujino., M, Ishikawa., "Numerical Analysis of Effects of Liquid Particles on Plasmadynamics in a Large-Scale Pulsed MHD Generator," AIAA Paper 2004–2369, June 2004.

[22] Mizukoshi, R., Matsumoto, Y., Fujino, T., and Ishikawa, M., "Design and Performance Analysis of Large Scale Nonequilibrium Disk MHD Generator," AIAA Paper 2007–4241, June 2007.

[23] Bityurin, V. A., and Bocharov, A. N., "MHD Flow Control in Hypersonic Flight," *Proceedings of Fifteenth International Conference on MHD Energy Conversion and Sixth international Workshop on Magnetoplasma Aerodynamics*, Vol. 2, Inst. of High Temperatures, Russian Academy of Sciences, Moscow, 2005, pp. 429–433.

[24] Otsu, H., Atsushi, M., Takashi, A., and Konigorski, D., "Feasibility Study on the Flight Demonstration for a Reentry Vehicle with the Magnetic Flow Control," AIAA Paper 2006–3566, June 2006.

A. Gallimore
Associate Editor